Defect-Rich Graphdiyne Quantum Dots as Efficient Electron-Donors for Hydrogen Generation

Wahid Ullah, Amine Slassi, Cong Wang, Erwan Paineau, Minh-Huong Ha-Thi, Thomas Pino, Zakaria Halime, Audrey Gayral, Maxime Vallet, Jéril Degrouard, Jérôme Cornil, and Mohamed Nawfal Ghazzal*

Downsizing the graphdiyne (GDY) network to shape quantum dots (QDs) will provide attractive optical and electronic properties associated with quantum confinement and edge effects. Here, it is demonstrated that quantum confinement and defect introduction allow using GDY in donor–acceptor photocatalytic systems for solar-to-hydrogen conversion. The defect-rich GDY QDs (GDYO-QDs) exhibit a blue-to-green excitation-dependent photoluminescence behavior, demonstrating their ability to harvest light over a wide energy range. Quantum-chemical calculations evidenced an increase in the electronic bandgap of GDY upon quantum confinement and defect introduction without the appearance of trap states that can hamper charge transport properties. Such a unique optical behavior of QDs is used in photocatalytic hydrogen generation through the hybridization with TiO_2 as a model photocatalyst. Theoretical and experimental results demonstrate that the donor–acceptor system tremendously boosts the photocatalytic performance, reaching 5288 $\mu mol\ g^{-1}$ after 4 h of illumination at a constant rate of 1322 $\mu mol\ g^{-1}\ h^{-1}$, using a low volume of a sacrificial electron donor (6% v/v). The QDs act as efficient chromophores harvesting UV and visible light while injecting electrons into the TiO_2. This work opens a new area of using GDYO-QDs as an efficient chromophore in developing donor–acceptor systems for photocatalysis and future photovoltaic devices.

1. Introduction

Graphdiyne (GDY) is an emerging 2D carbon allotrope consisting of alternated hybridized orbitals (sp and sp^2) arranged in a highly ordered honeycomb lattice structure that is predicted to exhibit unique electronic properties.[1–3] The structure provides GDY with a highly rich π-conjugated scaffold, uniform pores distribution, high surface area, and high carrier mobility, enabling efficient charge transport, which can be utilized for various catalytic processes.[4,5] Unlike graphene, a zero-bandgap material, the presence of carbon–carbon triple bonds introduces a bandgap in the electronic structure, allowing it to have semiconductor behavior and a tunable bandgap.[6] While GDY was mainly used as a support for electrocatalytic or catalytic reactions,[7,8] the opportunity to tune the bandgap has extended its use to energy related applications. The heteroatom doping, covalent and

W. Ullah, C. Wang, A. Gayral, M. N. Ghazzal
Université Paris-Saclay
UMR8000 CNRS
Institut de Chimie Physique
Orsay 91405, France
E-mail: mohamed-nawfal.ghazzal@universite-paris-saclay.fr

A. Slassi
ENS
LIRBEM
Cadi Ayyad University
Marrakech 40000, Morocco

A. Slassi, J. Cornil
Laboratory for Chemistry of Novel Materials
University of Mons
Place du Parc 20, Mons 7000, Belgium

E. Paineau, J. Degrouard
Université Paris-Saclay, CNRS
Laboratoire de Physique des Solides
Orsay 91405, France

M.-H. Ha-Thi, T. Pino
Université Paris-Saclay, CNRS
Institut des Sciences Moléculaires d'Orsay
Orsay 91405, France

Z. Halime
Université Paris-Saclay, CNRS
Institut de Chimie Moléculaire et des Matériaux d'Orsay
Orsay 91405, France

**ADVANCED
SCIENCE NEWS**

www.advancedsciencenews.com

**ADVANCED
ENERGY
MATERIALS**

www.advenergymat.de

non-covalent molecular functionalization allowed tailoring the electronic properties and increasing the number of active sites.[9–20] A bottom-up method, aiming at H-substitution of the diacetylenic groups in the ortho and para position of the benzene rings of the conjugated network, has been proposed to open the GDY bandgap and reach optimal interfacial charge separation and photocatalytic H_2 generation.[21] The H-graphdiyne has also been demonstrated to be promising as an electrode material for hydrogen and oxygen evolution reactions.[22–24] Despite the huge efforts made at exploring GDY as an attractive platform possessing tunable electronic properties, several challenges associated with GDY-size dependent properties are still to be addressed.[25,26] The morphology, size, thickness, and number of layers of 2D nanosheets greatly influence their physical and chemical properties. Thus, downsizing a 2D carbon-based network to a finite size below 100 nm to shape QDs provides attractive optical and electronic properties associated with quantum confinement and edge effects.[27] In particular, the QDs exhibit a size-dependent bandgap behavior and higher absorption capability over wider spectral regions,[28] which is strongly desirable in solar energy applications. Carbon based-QDs can be used to fabricate solar cells or interfaced as photosensitizers with metal oxides, giving rise to visible-light photocatalytic and photovoltaic devices.[29] On this aspect, graphdiyne is yet to be fully explored to adopt structural rescaling and quantum confinement methods. Indeed, quantum confined materials could exhibit highly demanded optical properties and even generate hot electrons and holes that are key species in efficient photoredox reactions. To the best of our knowledge, graphdiyne quantum dots with tunable optical properties were mainly reported for their photoluminescent properties for biological detection applications.[30,31]

In this work, we report the effect of quantum confinement of GDY with narrow size distribution on their optical, electronic, and photocatalytic properties. The GDYO-QDs were obtained using oxidative method, allowing the introduction of defects (functional groups) that provide the GDYO-QDs with the ability to absorb solar light in a wide spectral range. Indeed, QDs exhibit an excitation-dependent PL behavior, shifting from blue to yellow as the excitation wavelength changes. The photoluminescence response translates the generation of discrete electronic levels. The GDYO-QD with extended π-electron systems was hybridized with a TiO_2 surface as a photocatalyst model to construct a donor−acceptor system and demonstrate the use of GDYO-QDs as electron donor (chromophore) for photocatalytic H_2 generation. Quantum confinement is expected to increase the

electronic coupling between GDYO-QDs and TiO_2. At optimal loading, the GDYO-QDs/TiO_2 photocatalyst exhibited excellent donor–acceptor ability, where QDs were able to improve the photosensitization by increasing the light-harvesting capability and boosting the photocatalytic performance, using a low amount of sacrificial electron donor. The photocatalytic H_2 production was 23 times higher than pristine TiO_2. This work report on the use of GDYO-QDs as an efficient chromophore and electron donor for photocatalytic H_2 generation.

2. Results and Discussion

The synthesis of GDYO-QDs is achieved through a top-down two-step process, which starts by cutting the pre-synthetized pristine GDY films, as shown in **Figure 1a**. The morphology changes occurring during the two-step process were analyzed by transmission electron microscopy (TEM) and reported in Figures 1 and S1 and S2 (Supporting Information). The GDY, previously grown and peeled off from the Cu substrate, was oxidized in an acidic mixture of H_2O_2/H_2SO_4. The GDY and defect-rich GDY exhibit 2D sheet morphology, yet the layers in the GDY film are more compact than in GDYO (Figure S1e–h, Supporting Information). Essentially, the oxidation process exfoliates the GDY to a few transparent layer sheets with crinkles, folds and atomic arrangement visible in Figure S1e–h (Supporting Information). Then, the size of the GDYO film was further reduced using sonication for 1 h, followed by hydrothermal treatment (more details are reported in the supporting information). The hydrothermal treatment allows cutting GDYO and forming GDYO-QDs with a 5–6 nm diameter and atomic spacing of 0.38 nm, as shown in the high-resolution TEM Figures 1b–f and S2 (Supporting Information). The size of QDs and the atomic arrangement are in agreement with previous studies.[30] The as-prepared GDYO-QDs are highly stable in solution, and no precipitation was observed over days of aging.

The bonding structure of GDY-based materials was characterized by Raman spectroscopy, and the results are shown in **Figure 2a**. The Raman spectroscopy revealed four bands typical of pristine GDY, which are D (1385.5 cm^{-1}), G (1566.7 cm^{-1}) bands of sp^2 bonded carbon atoms of aromatic rings, and two vibrations corresponding to the sp hybridized carbons of the diacetylenic group centered at 1934 and 2182.8 cm^{-1}. The relatively low ratio of I_D/I_G (0.81) points toward fewer defects and a high degree of structural organization of the GDY.[1] The successive oxidation, exfoliation, and hydrothermal treatment lead to GDYO-QDs that also display D and G bands at 1385.5 and 1566.6 cm^{-1} (green curve in Figure 2a), yet with higher I_D/I_G ratio ($\approx$1), indicating an increase of defects in the structure. The peaks associated with sp hybridized carbons significantly decrease, suggesting preferential oxidation on the acetylenic bonds. Additionally, a higher background originating from strong fluorescence activity of the QDs over a wide spectral region during the Raman spectra acquisition overlapped with the signal of the acetylenic group, thus suppressing the Raman signals.[32] The chemical structures and the appearance of polar functionalities in the QDs were also confirmed by Fourier Transform Infrared (FTIR) spectroscopy (Figure S3, Supporting Information). The peaks at 1426, 1593, 1717, 2920, and 3415 cm^{-1} are assigned respectively to C−OOH, C=C, C=O, C−H, and O−H functions. Nevertheless, compared to GDY, the

M. Vallet
CentraleSupélec
ENS Paris-Saclay
CNRS
LMPS -Laboratoire de Mécanique Paris-Saclay
Université Paris-Saclay
Gif-sur-Yvette 91190, France

M. Vallet
Université Paris-Saclay
CNRS
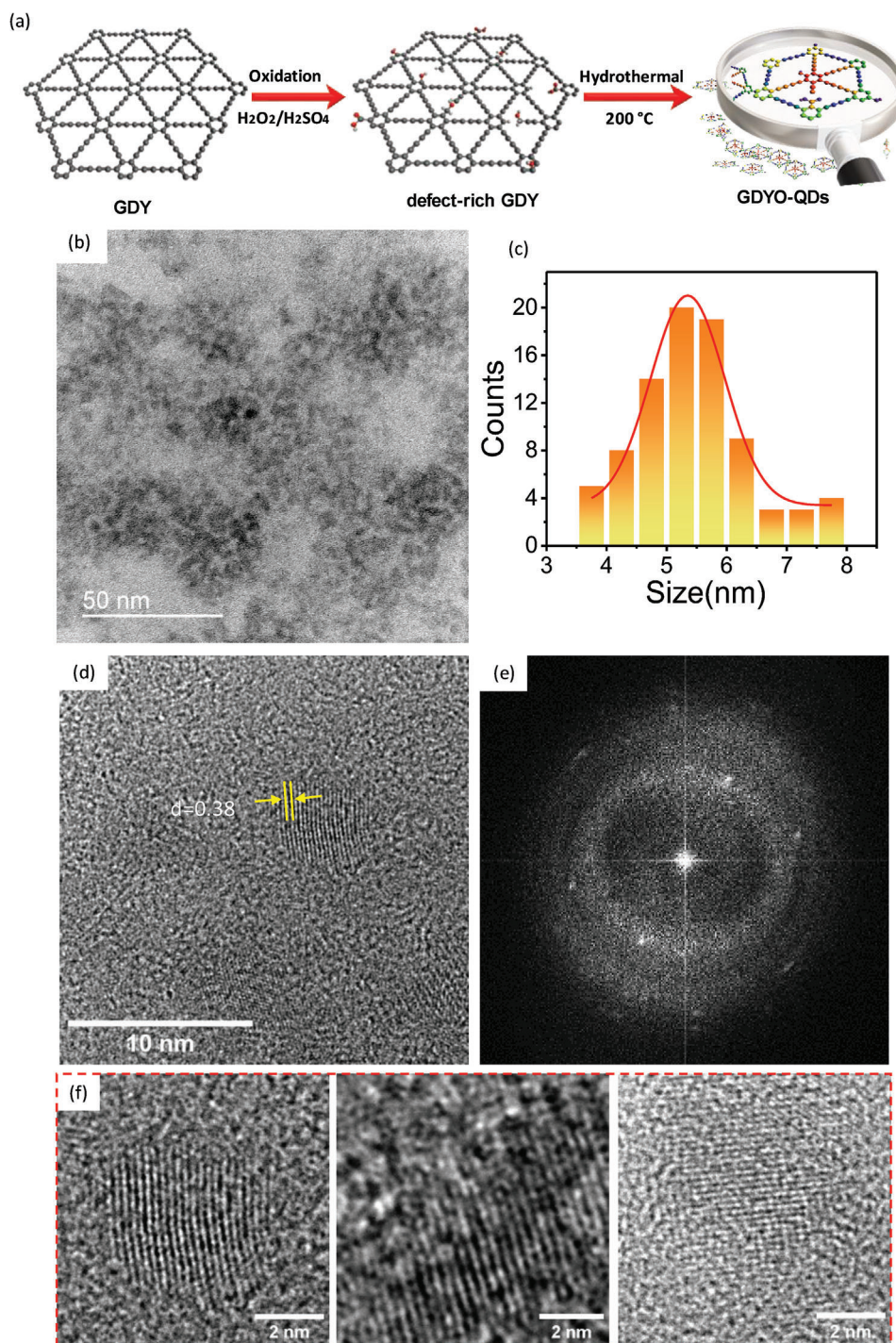Laboratoire SPMS
CentraleSupélec
Gif-sur-Yvette 91190, France

Figure 1. a) Schematic illustration of the experimental part for the GDYO-QDs. b,c) TEM images of GDYO-QDs and the corresponding size distribution. d,e) HR-TEM images of QDs with atomic arrangement and their Fast-Fourier-transform (FFT). f) HR-TEM images showing single GDYO-QDs.

oxide and QDs samples exhibited supplementary intense bands associated with bonded oxygen, indicating the successful chemical oxidation of the GDY surface, in agreement with previous studies.[33] X-ray photoelectron spectroscopy (XPS) was used to investigate the chemical surface composition of GDY and GDYO-QD. The high-resolution C 1s spectra of GDY (Figure S4, Supporting Information) are deconvoluted into four sub-peaks assigned to C=C (284.55 eV), C≡C (285.3 eV), C—O (286.6 eV) and C=O (288.2 eV). The ratio of sp/sp^2 carbon peaks is ≈2, pointing to a high degree of structural organization and interconnection of benzene rings through the acetylenic linkages.[34] The oxidation of GDY induces a chemical shift of the peak at 285 eV, and
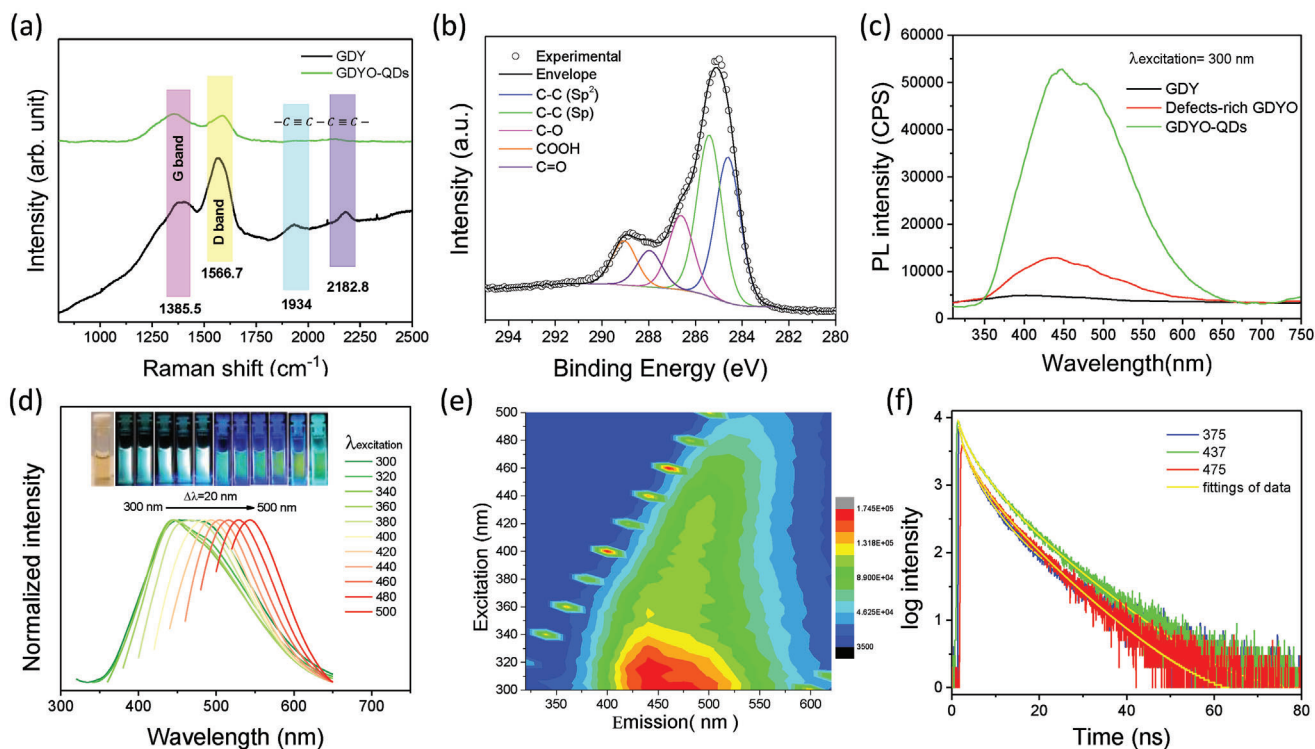
**ADVANCED
SCIENCE NEWS**

www.advancedsciencenews.com

**ADVANCED
ENERGY
MATERIALS**

www.advenergymat.de

Figure 2. Structural and optical characterization. a) Raman analysis of GDY and GDYO-QDs, b) high resolution C 1s X-ray photoelectron spectroscopy (XPS) data of GDYO-QDs, c) comparison of photoluminescence (PL) spectra of GDY, GDYO and GDYO-QDs, d) excitation dependent PL spectra of GDYO-QDs and image visualization of the fluorescence at the corresponding wavelengths shown in the inset, e) emission-excitation intensity 3D mapping and f)TR-PL fitted decay curves of GDYO-QDs, recorded at three different λ_{ex}.

the appearance of a shoulder centered at 289 eV (Figure 2b) assigned to the generation of O=C–O functional groups. Notably, the ratio of the peaks area of sp/sp^2 bonded carbon decreased upon oxidation. The weakening of the sp-carbon signal indicates a preferential breaking down of acetylenic groups compared to benzene rings during oxidation.

The optical properties of the as-synthesized GDYO-QDs were evaluated using UV–vis and photoluminescence spectroscopies. The QDs showed a shifted absorbance to higher energy, compared to GDY and defects-rich GDY (Figure S5, Supporting Information). Even though the QDs showed a broad absorption in the UV–vis spectral region, they left behind a tail-like decay in the near infra-red region. This originates from the electronic transitions between π–π^* and n–π^* of C=C, C≡C, and C=O bonded atoms of the GDYO-QDs skeleton. The photophysical processes in QD materials need comprehensive insight and detailed understanding. In defective QDs, surface states play a significant role not only in charge carriers' dynamics but also in influencing the fluorescence properties, for example, photoluminescence (PL) quenching and enhancement and inter and intra-molecular charge transfer mechanisms.[35] Detailed PL analyses were conducted to gain a better insight into the quantum confinement and surface state defects of GDY-QDs. The PL response of the GDYO-QDs exhibits very high photoemission compared to GDY and GDYO with a broad emission peak, shifting 50 nm away from the GDY peak, as shown in Figure 2c. The changes in the optical response and peak shift upon material hammering are attributed to the chemical modification of the GDY skele-

ton by oxy-functional groups, size rescaling, and layer exfoliation. We further explored the effect of the formation of these functional groups (defects) on the optical properties of GDYO-QDs by recording the PL emission spectra at various excitation wavelengths ($\lambda_{ex.}$) ≈300–500 nm (Figure 2d). Initially, by varying the $\lambda_{ex.}$ from 300 to 360 nm, the emission peak remains unchanged and centered at 460 nm. However, monitoring the $\lambda_{ex.}$ in the 380–500 nm range revealed a gradual red shift of the PL emission peak. Nevertheless, the intensity of peak maxima also decreases, which could indicate faster non-radiative recombination as expected from increasingly small gaps. The excitation-dependent optical behavior is further visualized in the recorded images (see inset of Figure 2d) at different wavelengths, displaying color variations from blue to green under monochromatic light following the trend of PL emission spectra. The fluorescence behavior is supported by 3D emission-excitation displayed in Figure 2e. The cartography gives a visualization of the relationship between excitation and emission, demonstrating that the QDs can be excited through a wide range of energy and yet show a large window of spectral emission with variable intensity. It is worth mentioning that some small islands are also visible on the left side of the main 3D mapping related to Rayleigh scattering due to high order scattering from the monochromator. The excitation-dependent fluorescence is attributed to the quantum confinement and the defects generated during the preparation of GDYO-QDs.[36,37] We also conducted time-resolved photoluminescence (TR-PL) experiments, as shown in Figure 2f, to understand the recombination dynamics of GDYO-QDs by applying three different excitation
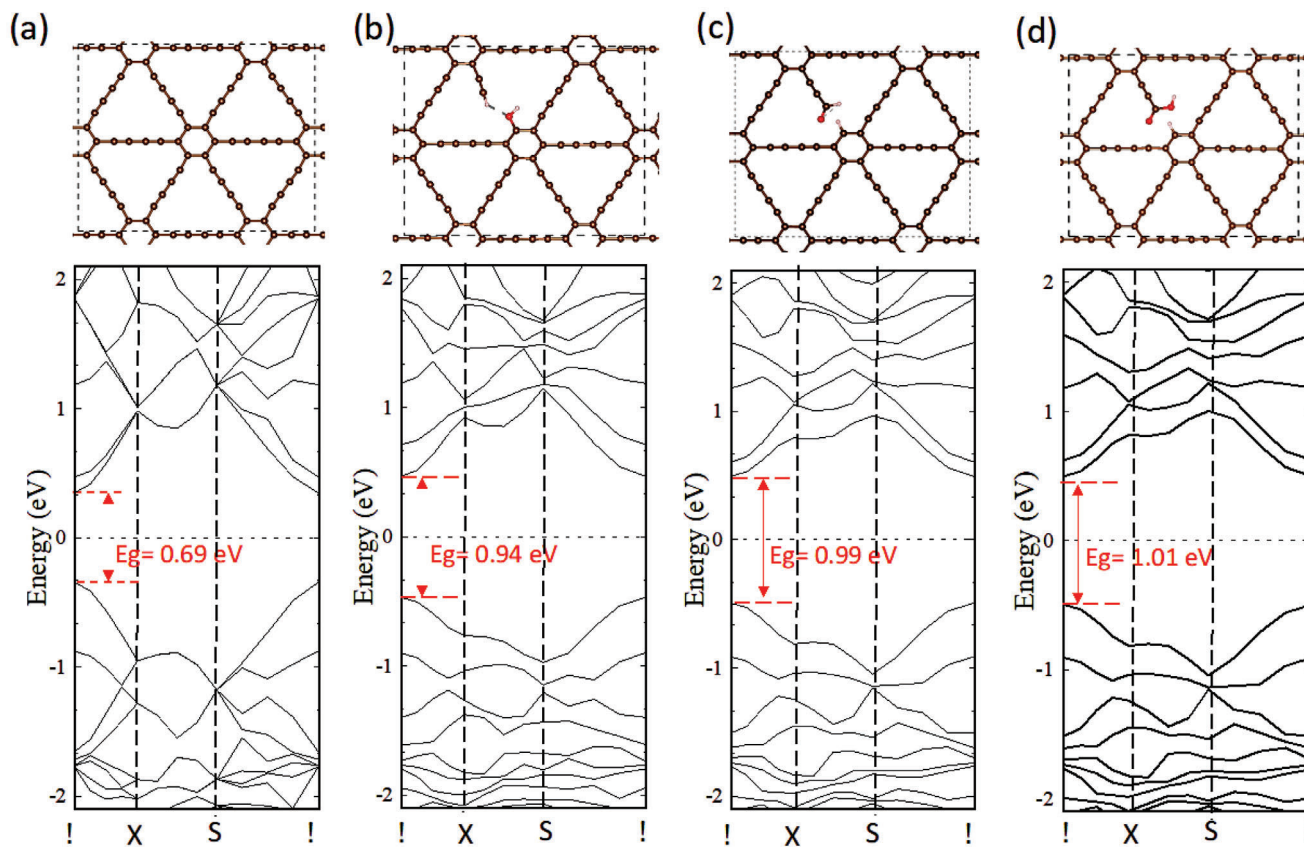
Figure 3. Top view of representative adsorption configurations of oxygenated functional groups and their band structures calculated at DFT/HSE level. The band structures of additional configurations are shown in Figure S8 (Supporting Information).

wavelengths (375, 437, and 475 nm) while emission was adjusted according to the steady state PL from Figure 2d. The decay curves have almost the same intensity and are superimposed on each other. The data fitted well with triexponential decay functions, and the lifetime parameters are tabulated in supporting information (Table S1, Supporting Information). The first decay τ_1 of GDYO-QDs is short and likely originates from the emission of intrinsic states of the GDY configuration. The relatively longer decay components (τ_2 and τ_3) are associated with various phenomena, including defects or functional groups (OH, COOH, and CO, etc.) on the surface of GDYO-QDs, quantum confinement effect, and surface traps.[38] These results also support the FTIR (Figure S3, Supporting Information) and XPS (Figure 2b) analysis, indicating the generation of functional groups on the QDs surface. This is also in agreement with PL emission spectra (Figure 2d) and photoluminescence excitation (PLE) results (Figure S6, Supporting Information). The excited carriers were reported to be confined to the surface sites, making the surface defect fluorescence dominant so that increasing λ_{ex} yields a noticeable red shift.[39] Similarly, the GDYO-QDs contain a mixture of hybridized carbon (i.e., sp^2 and sp) compared to other carbon materials, creating several surface states that can equally alter the PL properties of GDYO-QDs.

To further rationalize the experimental data, Density Functional Theory (DFT) calculations with periodic boundary conditions were carried out to evaluate the impact of the formation of

oxygenated functional groups (OH, COOH, and COH) revealed by FTIR and XPS on the properties of the GDY and hybrid systems made with TiO_2. First, we started our calculations by seeking the stable adsorption configurations of the oxygenated functional groups (OH, COOH, and COOH) on defective GDY with two/four carbon vacancies in the acetylene linkages that were shown experimentally to be the most affected upon oxidation; in the following, the results with two carbon vacancies will be presented in the core of the article while those obtained with four carbon vacancies will be collected in the supporting information. The most stable adsorption configurations retained for our study are shown in Figure S7 (supporting information). It is found that the basal plane structure of the GDY layer is systematically preserved upon adsorption of the functional groups. The band structure computed for each system (**Figure 3**; Figure S8, Supporting Information) revealed that the adsorption of such oxygenated functional groups on GDY significantly opens its bandgap by 30%, from 0.69 eV (for GDY pristine) up to 1.01 eV (with functional groups). This is in total agreement with the blue shift of the absorption band of GDYO-QDs upon oxidation. Importantly, no trap states were observed within the bandgap, thus ensuring that the functionalization will not deeply affect the charge transport properties.

Next, we consider the heterostructure systems by placing GDY and its oxygenated counterparts on the main exposed (101) surface of TiO_2, which is non-polar. The optimized structures of the

ADVANCED
SCIENCE NEWS

www.advancedsciencenews.com
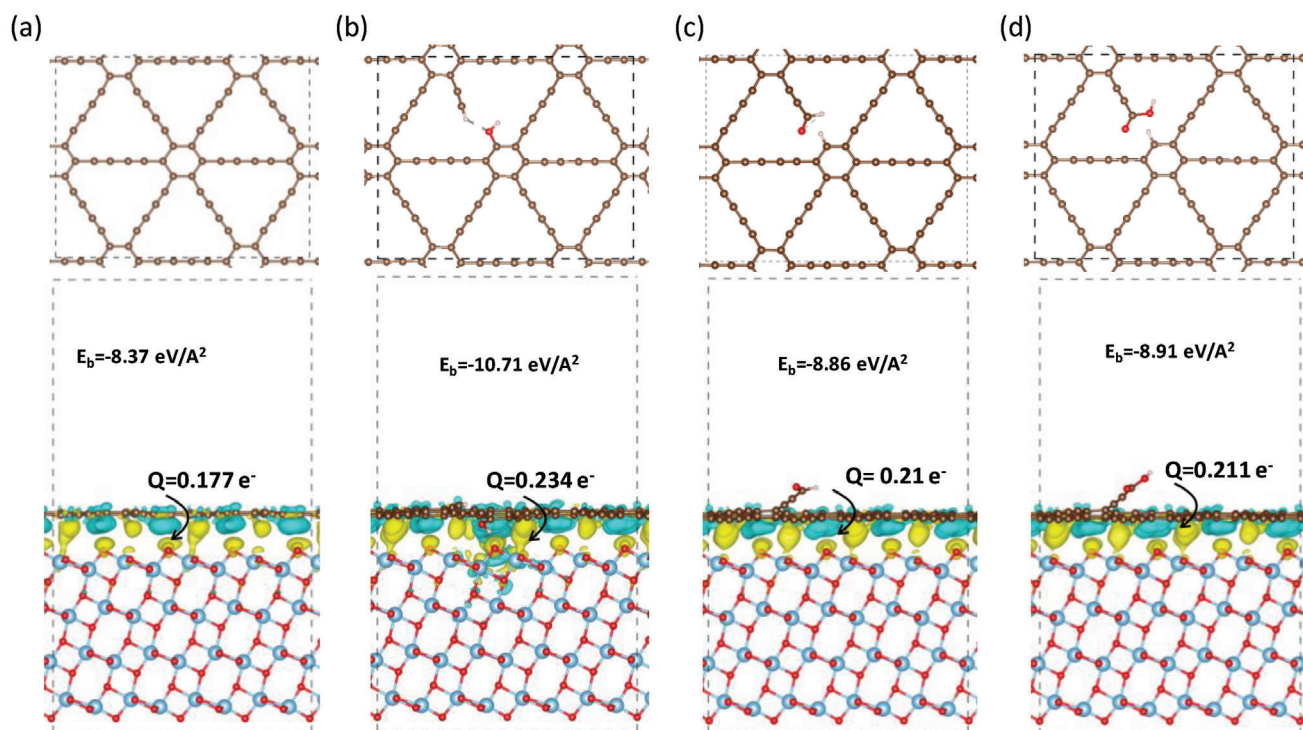
ADVANCED
ENERGY
MATERIALS

www.advenergymat.de

Figure 4. Equilibrium structure of the hybrid systems along with 3D density change difference for a) pristine GDY and defective GDY with oxygenated functional groups: b) −OH, c) −COH, and d) −COOH.

built GDYO-QDs/TiO$_2$ interfaces are shown in **Figures 4** and S9 (Supporting Information). Due to the large size of the systems, the binding energy was calculated at the DFT/PBE level by including van der Waals corrections using the following equation:

$$E_{int} = E_{tot} - E_{TiO_2} - E_{GDY} \qquad (1)$$

where E_{tot}, E_{TiO_2} and E_{GDY} are the total energies of the heterostructure, TiO$_2$ layer and GDYO-QDs layers in the different configurations, respectively, in the geometry of the interacting relaxed heterostructures. The equilibrium geometries of the heterostructures are given in Figures 4 and S9 (Supporting Information). The GDY monolayer can undergo a non-negligible buckling at the interfaces due to Coulomb attraction or repulsion between the oxygenated functions and the underneath atoms in the TiO$_2$ surface. As a matter of fact, some oxygenated functional groups, such as COH and COOH, move away from the GDYO-QDs surface due to repulsive interaction with oxygen atoms of the TiO$_2$ surface (Figure 4c,d). On the other hand, in the case of OH substitution, the hydrogen atom is attracted by oxygen atoms of the TiO$_2$ surface (Figure 4b). More importantly, the calculated binding energy values demonstrate that the adsorption of functional groups improves the adhesion energy of the heterostructure in each case, with the largest increase observed for the OH functionalization. The larger adhesion energy originates from a more pronounced charge transfer between TiO$_2$ and defective GDYs, thus yielding an extra Coulomb stabilization.

Capitalizing on their exceptional optical properties and ability to act as electron donors (chromophores) revealed by the DFT calculations (vide infra), we evaluated GDYO-QDs for photocatalytic H$_2$ evolution reaction by making hybrids with TiO$_2$-P25. To do so, various weight % (1, 2, 3, 5, and 10%) loading of QDs is hybridized with commercial TiO$_2$-P25 as model photocatalyst (experimental details are given in supporting information), and their photocatalytic efficiency is evaluated. The HR-TEM image in **Figure 5a** unveils the successful hybridization. The spherical QDs are attached to TiO$_2$ nanoparticles with 0.34 nm (101) lattice spacing (Figure S10, Supporting Information). The Wide-Angle X-ray scattering (WAXS) analysis of the nanostructure exhibits a mixture of anatase and rutile crystalline phase, typical of P25, without any significant change after the formation of QDYO-QDs/TiO$_2$ interface (Figure S11, Supporting Information). The high-resolution Ti 2p peaks centered at 459 and 464.7 eV are assigned to Ti 2p$_{3/2}$ Ti 2p$_{1/2}$, respectively, with a satellite contribution at 472 eV (Figure 5b). It is obvious that with increasing GDYO-QDs content loading, the peak intensities gradually decrease. A slight positive shift at Ti 2p$_{3/2}$ is also noticeable, attesting to the strong interaction with TiO$_2$, which is in agreement with DFT calculations. The high-resolution C 1s peak in Figure 5c presents identical contributions as previously observed for pure GDYO-QDs (Figure 2b), pointing to the preservation of GDYO-QDs skeleton after hybridization, also in agreement with TEM observations. Moreover, surface crystallinity, defects, and hybridization of the GDYO-QDs/TiO$_2$ were also elaborated by employing Raman vibrational spectroscopy (Figure 5d). Under the illumination by a laser source at 532 nm, pure TiO$_2$ projected with several Raman bands ≈138.4, 394.4, 514.2, and 636.8 cm^{-1} respectively assigned to the $E_{g(1)}$, $B_{1g(1)}$, A$_{1g}$ + B$_{1g(2)}$, and $E_{g(3)}$ symmetries of TiO$_2$ anatase modes (Figure 5d).

**ADVANCED
SCIENCE NEWS**

www.advancedsciencenews.com

**ADVANCED
ENERGY
MATERIALS**
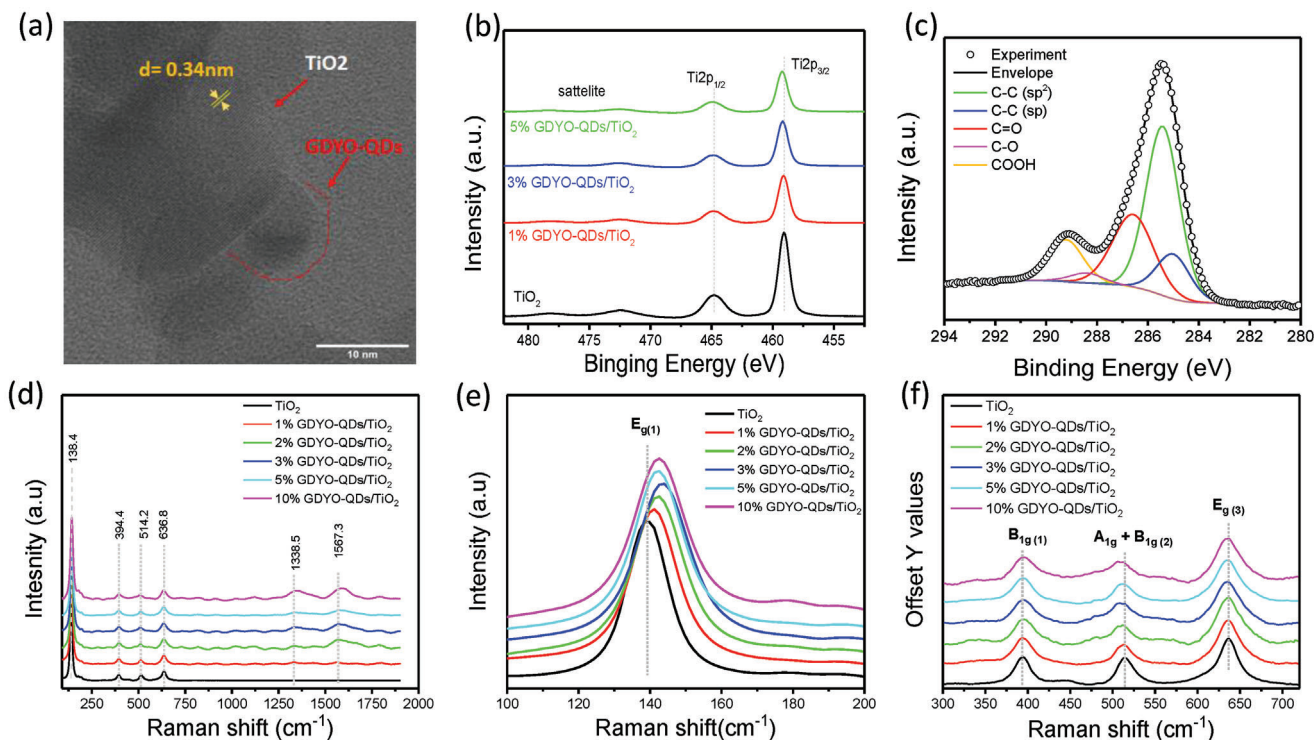
www.advenergymat.de

Figure 5. Morphological and structural characterization of GDYO-QDs/TiO$_2$ samples. a) HR-TEM, b,c) high-resolution Ti 2p and C 1s XPS spectra, respectively, d) Raman vibration of GDYO-QDs/TiO$_2$, and e,f) high magnification of characteristic Raman vibration modes.

GDYO-QDs/TiO$_2$ hybrid samples also exhibit the typical anatase Raman vibration modes with two additional peaks at 1338.5 and 1567.3 cm^{-1} corresponding to the D and G bands of GDYO-QDs; they become more prominent with increasing QDs concentration, thus confirming the hybridization between GDYO-QDs and TiO$_2$ nanoparticles. This confirms that the anatase phase of TiO$_2$ and the main structure of GDYO-QDs remains intact in the composites. Nevertheless, compared to the peaks of free TiO$_2$, the main peak $E_{g(1)}$ in GDYO-QDs/TiO$_2$ hybrids is gradually red shifted from 138 to 143 cm^{-1}. Similarly, the A_{1g} + $B_{1g(2)}$ modes are also projected with a slight shift from 514.2 to 508.6 cm^{-1} with increasing QDs wt%, as shown in the high magnification views of Raman curves in Figure 5e,f. These Raman bands reveal a strong interaction between GDYO-QDs and TiO$_2$ nanocrystals.[40] A shift to lower wavenumber also suggests a weakening of the Ti-O bonds, which may be due to electron transfer from GDYO-QDs to TiO$_2$.[41] It is worth mentioning that the noisy background and fringes in the Raman curves of hybrid samples are due to the interference of strong emission from the fluorescent GDYO-QDs. Similarly, FTIR spectra of the GDYO-QDs/TiO$_2$ displayed a strong band between 450–870 cm^{-1} region associated with Ti—O—Ti/Ti—O—H stretching mode, consistent with Raman results, and the peaks ≈1622 and 3400 cm^{-1} are respectively the classical Ti—OH stretching and O-H vibration (Figure S12a, Supporting Information). The GDYO-QDs/TiO$_2$ composites also exhibited extra peaks of the GDYO-QDs skeleton ≈1200, 1380, and 1550 cm^{-1} originating from the C—OH, C=O, and C=C vibration modes, respectively. The absorption band of TiO$_2$ is affected by interfacing GDYO-QDs, as shown by UV–vis

spectra (Figure S12b, Supporting Information). With the incorporation of GDYO-QDs, the absorption range is extended toward lower energy, and the absorption intensity gradually increases as the amount of QDs content increases.

The photocatalytic hydrogen generation was performed under UV–vis and visible light (>400 nm) excitations in aqueous solutions containing 6% in volume of triethanolamine (TEOA) as a sacrificial electron donor (**Figure 6**). Interfacing GDYO-QDs with TiO$_2$ shows a remarkable enhancement of the photocatalytic H$_2$ generation. The optimal weight ratio of the QDs was 1–2 wt%. The hydrogen generation, which was relatively low for the pristine TiO$_2$, reaches a total amount of ≈5288 µmol g^{-1} for 1% GDYO-QDs/TiO$_2$ after 4 h of illumination (Figure 6a), corresponding to an average ≈1322 µmol h^{-1} g^{-1} H$_2$ production rate. The amount of H$_2$ remained unchanged up to 2 wt% of QD loading, indicating a saturation in terms of photocatalytic activity. Nonetheless, further increase in GDYO-QDs concentration (≈3, 5, and 10 wt%) has an inverse effect by gradually decreasing the amount of H$_2$ generation to 2429 µmol g^{-1} for 10% GDYO-QDs/TiO$_2$, after 4 h irradiation, at an average rate of 607 µmol h^{-1} g^{-1} (Figure 6b), even though, the H$_2$ production remains much higher compared to non-modified TiO$_2$. These results indicate that a maximum coverage of the TiO$_2$ surface is reached at 2 wt% while increasing the number of QDs at the surface beyond this threshold probably blocks active sites where the reduction reaction occurs, decreasing thus the H$_2$ production. The stability of the composite was also assessed through cycling experiments, and the results show only 17% decrease after four consecutive cycles, indicating the hybrid material long-lasting stability and
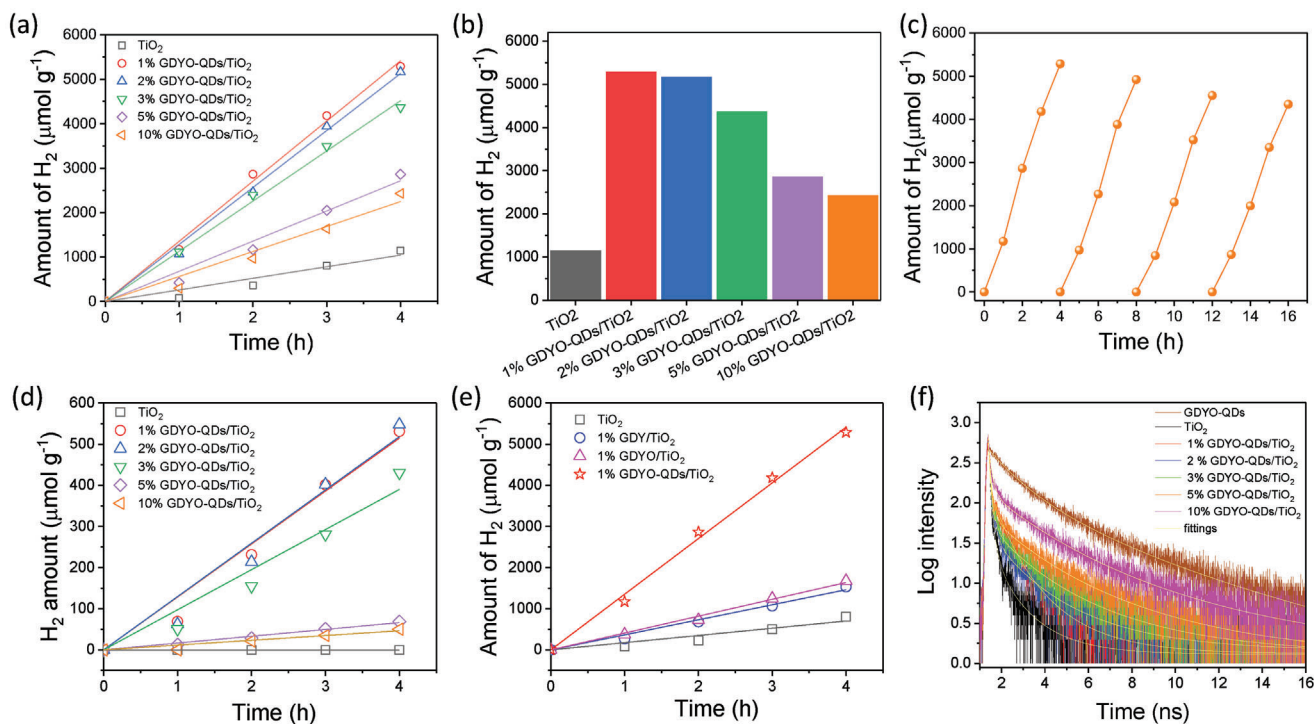
Figure 6. Photocatalytic hydrogen generation over commercial TiO$_2$-P25 and our fabricated GDYO-QDs/TiO$_2$ hybrid photocatalysts; a) time-coursed H$_2$ generation under the illumination with UV–vis light over different photocatalysts using 6% (v/v) triethanolamine as sacrificial electron donor, b) comparison of the amount of H$_2$ produced, for different photocatalysts, after 4 h of irradiation, c) cyclic activity of 1%GDYO-QDs/TiO$_2$ photocatalyst for H$_2$ generation, d) time-coursed H$_2$ production under visible light (>400 nm) over TiO$_2$-P25 and GDYO-QDs/TiO$_2$ hybrid photocatalysts, e) comparison of the photocatalytic H$_2$ generation with TiO$_2$-P25, 1% GDY/TiO$_2$, 1% defects-rich GDY/TiO$_2$ and 1% GDYO-QDs/TiO$_2$ hybrids f) time-resolved PL decays of the control and hybrids samples recorded at λ_{em} 430 nm using excitation source λ_{ex} 373 nm.

durability for the hydrogen evolution reaction (Figure 6c). Previously, we observed that GDYO-QDs are also capable of harvesting visible light, predominantly attributed to the quantum confinement effect and surface defects in the materials and, therefore, of generating electrons that can be injected into the host TiO$_2$ surface. Under visible light illumination at $\lambda > 400$ nm (Figure 6d), the QDs/TiO$_2$ hybrid samples exhibit significant photocatalytic activity for H$_2$ production compared to TiO$_2$-P25 alone. Indeed, P25 shows no activity under visible light, while an average rate of 132.7 µmol h^{-1} g^{-1} was obtained for 1% GDYO-QDs/TiO$_2$. Moreover, the photocatalytic activity trend is similar to what has been observed under UV–vis light excitation. GDY and GDYO were hybridized with TiO$_2$ under an optimal ratio of 1 wt%, and their activities were compared to GDYO-QDs. GDY and its oxidized form exhibited similar photocatalytic H$_2$ evolution, as shown in Figure 6e. Although the photocatalytic activity of TiO$_2$ improves, it remains far below the efficiency of 1% GDYO-QDs/TiO$_2$. The photocatalytic H$_2$ evolution performance of GDYO-QDs/TiO$_2$ is benchmarked against previously reported GDY-based composites outlined in Table S2 (Supporting Information). Despite employing merely 1 wt% of QDs and a sacrificial electron donor concentration half of that used in comparable studies, this metal-free hybrid photocatalyst exhibited remarkable H$_2$ production capabilities. These findings underscore the important role of GDYO-QDs in facilitating photosensitization and electron injection within the TiO$_2$ matrix, crucial for efficient H$_2$ production.

To further investigate the hybrid photocatalyst performance, we employed photoelectrochemistry to determine the light-dependent response by recording their transient photocurrent under monochromatic light excitation, $\lambda_{ex} \approx 300$–540 nm (Figure S13, Supporting Information). Initially, by increasing the λ_{ex}, the photocurrent intensities increased for all samples. TiO$_2$-P25 absorbs light in the UV region, and here, the maximum photocurrent for bare TiO$_2$ was reached at $\lambda_{ex} = 360$ nm and started to decrease with further increment in λ_{ex}. Instead, our GDYO-QDs/TiO$_2$ exhibited higher photocurrent intensity and significant light absorption capability over a wider spectral region from UV to visible. However, note that the photocurrent, in the case of higher GDYO-QD (5% and 10%) concentration, decreased again, similarly to what we observed during photocatalytic measurements. The single wavelength based photoelectrocatalytic behavior of GDYO-QDs follows exclusively the photocatalytic trends and highlights the role of GDYO-QDs in the light harvesting process. An apparent quantum efficiency of 3.87% is achieved for 1% GDYO-QDs/TiO$_2$ when irradiated at 400 nm wavelength using a monochromator (calculation details are given in section 1.5 supporting information). Moreover, the charge separation and transfer efficiency of the GDYO-QDs/TiO$_2$ was also probed by recoding electrochemical impedance spectroscopy (EIS) under simulated solar light in the frequency range of 10^5–0.1 Hz at open circuit potential. The EIS Nyquist plot, fitted with an equivalent circuit (inset), is shown in Figure S14 (Supporting Information), and the obtained resistance parameters are tabulated in Table S3
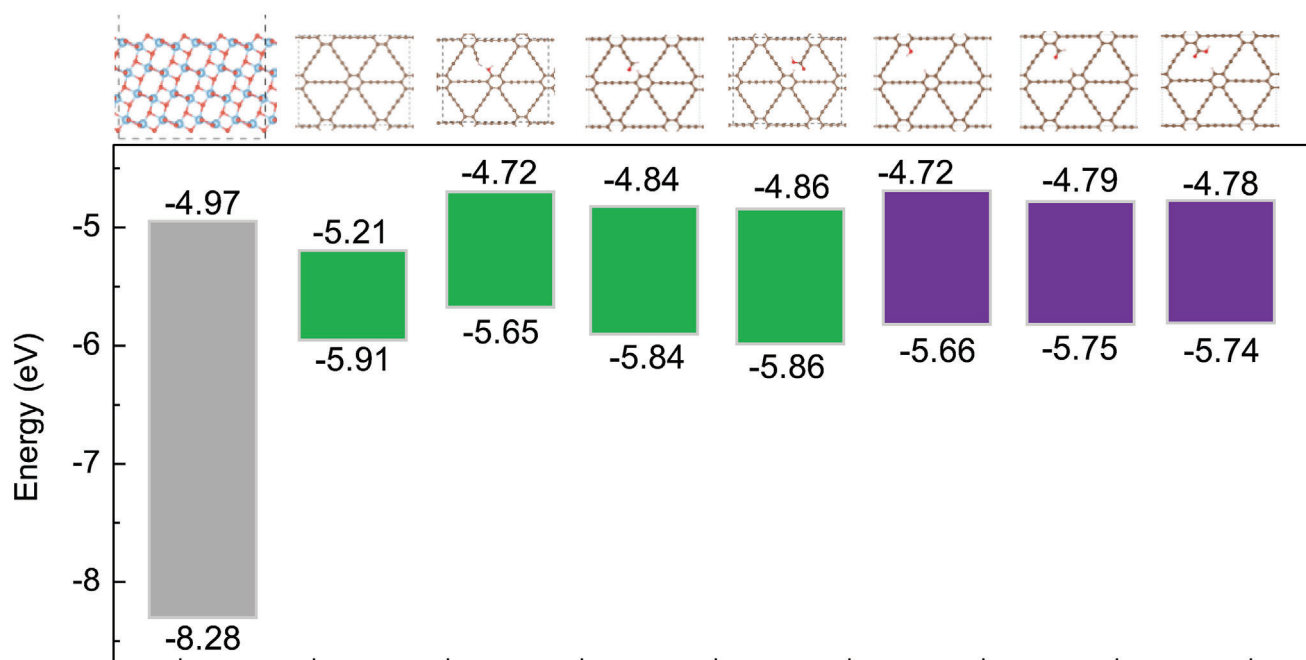
Figure 7. Band alignment of the isolated components calculated at the DFT/HSE level. The energy values are defined with respect to the vacuum level.

(Supporting Information). The semicircles radius of the Nyquist plot of all GDYO-QDs/TiO$_2$ hybrids are significantly smaller than that of pure TiO$_2$-P25, demonstrating that the hybrids experience lower charge transfer resistance, which facilitates the photogenerated charge carrier dynamics and electron-hole separations. The solution resistance (Rs) values did not significantly differ because the tests were performed in the same bulk electrolyte solution (Table S3, Supporting Information).[42] However, the charge transfer resistance (Rp) values rapidly decreased with 1% GDYO-QDs hybridization, pointing to the fast charge transfer process at the electrode surface.

The substantial rise in photocatalytic performance matches the capability of GDYO-QDs to harvest a wide range of UV–vis light. To further understand the photocatalytic activity of GDYO-QDs/TiO$_2$ hybrids, the PL emission spectra were recorded for GDYO-QDs/TiO$_2$ and are shown in Figure S15 (Supporting Information). The samples exhibit ≈8 nm peaks shift compared to TiO$_2$-P25, attributed to the interaction of QDs with the TiO$_2$ surface. The quantum confinement of GDYO-QDs bears several oxygen functional groups that allow the QDs grafting on the TiO$_2$ surfaces. This leads to the formation of GDYO-QDs/TiO$_2$ hybrids, which is in agreement with DFT calculations and the observed Raman shift. The emission signals were strongly quenched, ≈35%, in the presence of 1 wt% GDYO-QDs and up to 50% with 10 wt% QDs. This reflects the prolonged charge carrier lifetime in the GDYO-QDs/TiO$_2$ hybrids, pointing to the electron injection into the conduction band of TiO$_2$.

The electron injection mechanism from QDs to TiO$_2$ was assessed by titrating GDYO-QDs suspension against TiO$_2$ nanoparticles (aqueous dispersion). The PL behavior was recorded at 320 nm excitation wavelength, as shown in Figure S16 (Supporting Information). By adding TiO$_2$ aliquot, the PL emission intensities are gradually quenched with the increasing TiO$_2$ con-

centration, revealing the electron injection from GDYO-QDs to the TiO$_2$ photocatalyst, in agreement with TRPL results. To support this hypothesis and gain more insights on the carrier dynamics, we performed TRPL measurements of hybrids and the control samples (Figure 6f) at λ_{em} 430 nm and λ_{ex} 375 nm as source of energy. The curves were fitted with a tri-exponential decay function to obtain the decay parameters collected in Table S4 (Supporting Information). Compared to GDYO-QDs, the delay time of free TiO$_2$ is very short, indicating the fast recombination of photogenerated electron-hole pairs. In contrast, GDYO-QDs/TiO$_2$ samples exhibit intermediate decay curves, and an increasing trend is observed in the decay time (compare the average lifetimes in Table S4, Supporting Information) with a gradual increment of QDs wt%, also in line with the steady-state PL results. We also recorded the TRPL curves of hybrids and control sample (Figure S17, Supporting Information) with low energy excitation source ca. λ_{ex} 437 nm. The QDs/TiO$_2$ hybrid materials show significantly lower decay lifetime kinetics compared to QDs alone (Table S5, Supporting Information). The results indicate that once the QDs harvest light over a wider range, the excited electrons are injected into the conduction band of TiO$_2$ before relaxing to the ground state, in agreement with steady-state PL. **Figure 7** depicts the computed band alignment at the interface between TiO$_2$ and all GDYO-QDs monolayers. The results show that the bottom of the conduction band is raised in all defective GDY compared to the pristine system, which should facilitate electron transfer to the conduction band of TiO$_2$. Essentially, these QDs, with several surface functional groups, create defects, and a rich intrinsic π-conjugated configuration with the ability to capitalize on the donor–acceptor chemistry to establish a synergy with the TiO$_2$ crystals. Based on the above results, we proved successful at tuning the electronic properties of GDY using quantum confinement effects and by generating defects such

as functional groups at the surface. The GDYO-QDs possess the ideal electronic band structure to act as an efficient electron donor (chromophore) capable of injecting electrons to the CB of TiO_2 and thus improving its photocatalytic efficiency for hydrogen evolution reaction. After conducing these investigations, it is evident that GDYO-QDs are able to harvest the UV–vis light and photosensitize TiO_2 for H_2 generation. Our findings suggest a synergistic interplay between the constituents of the GDYO-QDs/TiO_2 hybrid under light irradiation, facilitating the generation and exchange of charge carrier. QDs harvest the light energy and generate excited electrons that are ultimately injected into the TiO_2 conduction band, allowing an efficient H^+/H_2 conversion reaction, as depicted in the schematic illustration provided in Figure S18 (Supporting Information).

3. Conclusion

To summarize, GDY is hammered by chemical oxidation and hydrothermal treatment to fabricate defect-rich GDYO-QDs of ≈5–6 nm diameter bearing several oxygen functional groups and displaying long-term stability and high solubility in water. The spectroscopic and microscopic methods employed in this study reveal the GDY surface functionalization and rescaling into QDs while retaining the main GDY structure. Compared to pristine GDY, the defects-rich GDYO-QDs displayed excitation-dependent photoluminescence from UV to visible range. Quantum-chemical calculations further support the interpretation of the experimental results. The introduction of oxygen functionalities are also found to increase the bandgap. We hybridized the QDs with commercial TiO_2-P25 nanoparticles at moderate experimental conditions to form a model GDYO-QDs/TiO_2 hybrid photocatalytic system. TEM, XPS, UV–vis, Raman, and FTIR and theoretical calculation provided important information on GDYO-QDs loading and surface interaction with TiO_2 nanoparticles. Steady-state PL and TRPL results reveal the electron injection occurred from QDs to TiO_2. The GDYO-QDs/TiO_2 hybrid exhibited promising photocatalytic hydrogen production in aqueous solution under UV–vis and visible light excitation. We reported 1322 µmol g^{-1} h^{-1} of hydrogen production rate with 1%GDYO-QDs/TiO_2 hybrid under UV–vis. The weight percent amount of GDYO-QDs in the composite is crucial for the photocatalytic activity. The higher amount of hydrogen production was obtained using only 1 wt% of GDYO-QDs. The visible light harvesting capability of GDYO-QDs allows extending the activity in the visible range, reaching a production H_2 rate of 132 µmol g^{-1} h^{-1}. This work opens a new area of using GDYO-QDs as an efficient chromophore, and its use could probably be extended to the development of future photovoltaic devices.

4. Experimental Section

The experimental details of GDY materials synthesis, characterization, and their computational details are listed in the supporting information.

Supporting Information

Supporting Information is available from the Wiley Online Library or from the author.

Conflict of Interest

The authors declare no conflict of interest.

Data Availability Statement

The data that support the findings of this study are available from the corresponding author upon reasonable request.

[1] G. Li, Y. Li, H. Liu, Y. Guo, Y. Li, D. Zhu, *Chem. Commun.* **2010**, *46*, 3256.

[2] D. Malko, C. Neiss, A. Görling, *Phys. Rev. B* **2012**, *86*, 045443.

[3] J. Li, X. Gao, L. Zhu, M. N. Ghazzal, J. Zhang, C.-H. Tung, L.-Z. Wu, *Energy Environ. Sci.* **2020**, *13*, 1326.

[4] C. Huang, Y. Li, N. Wang, Y. Xue, Z. Zuo, H. Liu, Y. Li, *Chem. Rev.* **2018**, *118*, 7744.

[5] B. Li, C. Lai, M. Zhang, G. Zeng, S. Liu, D. Huang, L. Qin, X. Liu, H. Yi, F. Xu, N. An, L. Chen, *Adv. Energy Mater.* **2020**, *10*, 2000177.

[6] D. Malko, C. Neiss, F. Viñes, A. Görling, *Phys. Rev. Lett.* **2012**, *108*, 086804.

[7] I. Muhammad, S. Ahmed, H. Cao, Z. Yao, D. Khan, A. Mahmood, T. Hussain, X.-G. Xiong, R. Ahuja, Y.-G. Wang, *Mater. Today Chem.* **2023**, *34*, 101756.

[8] X. Gao, H. Liu, D. Wang, J. Zhang, *Chem. Soc. Rev.* **2019**, *48*, 908.

[9] X. Zheng, X. Gao, R. A. Vilá, Y. Jiang, J. Wang, R. Xu, R. Zhang, X. Xiao, P. Zhang, L. C. Greenburg, Y. Yang, H. L. Xin, X. Zheng, Y. Cui, *Nat. Nanotechnol.* **2023**, *18*, 153.

[10] M. Cui, P. Xin, Z. Che, M. Zou, M. Zhang, X. Sun, Y. Yuan, Z. Zou, G. Lv, S. Wang, W. Hu, *Chem. Eng. J.* **2023**, *464*, 142629.

[11] S. C Shekar, R. S. Swathi, *Carbon* **2018**, *126*, 489.

[12] Z. Zhu, Q. Bai, S. Li, S. Li, M. Liu, F. Du, N. Sui, W. W. Yu, *Small* **2020**, *16*, 2001440.

[13] B. Liu, S. Zhan, J. Du, X. Yang, Y. Zhao, L. Li, J. Wan, Z.-J. Zhao, J. Gong, N. Yang, R. Yu, D. Wang, *Adv. Mater.* **2023**, *35*, 2206450.

[14] H. Bu, M. Zhao, H. Zhang, X. Wang, Y. Xi, Z. Wang, *J. Phys. Chem. A* **2012**, *116*, 3934.

[15] Y. Zhao, J. Wan, H. Yao, L. Zhang, K. Lin, L. Wang, N. Yang, D. Liu, L. Song, J. Zhu, L. Gu, L. Liu, H. Zhao, Y. Li, D. Wang, *Nat. Chem.* **2018**, *10*, 924.

[16] F. Wang, Z. Zuo, L. Li, K. Li, F. He, Z. Jiang, Y. Li, *Angew. Chem., Int. Ed.* **2019**, *58*, 15010.

[17] J. Xu, Q. Wan, M. Anpo, S. Lin, *J. Phys. Chem. C* **2020**, *124*, 6624.

[18] J. He, N. Wang, Z. Yang, X. Shen, K. Wang, C. Huang, Y. Yi, Z. Tu, Y. Li, *Energy Environ. Sci.* **2018**, *11*, 2893.

[19] C. Xie, X. Hu, Z. Guan, X. Li, F. Zhao, Y. Song, Y. Li, X. Li, N. Wang, C. Huang, *Angew. Chem., Int. Ed.* **2020**, *59*, 13542.

[20] T. Lu, J. He, R. Li, K. Wang, Z. Yang, X. Shen, Y. Li, J. Xiao, C. Huang, *Energy Storage Mater.* **2020**, *29*, 131.

[21] J. Li, A. Slassi, X. Han, D. Cornil, M. Ha-Thi, T. Pino, D. P. Debecker, C. Colbeau-Justin, J. Arbiol, J. Cornil, M. N. Ghazzal, *Adv. Funct. Mater.* **2021**, *31*, 2100994.

[22] T. Zhang, Y. Hou, V. Dzhagan, Z. Liao, G. Chai, M. Löffler, D. Olianas, A. Milani, S. Xu, M. Tommasini, D. R. T. Zahn, Z. Zheng, E. Zschech, R. Jordan, X. Feng, *Nat. Commun.* **2018**, *9*, 1140.

[23] X. Zhou, B. Fu, L. Li, Z. Tian, X. Xu, Z. Wu, J. Yang, Z. Zhang, *Nat. Commun.* **2022**, *13*, 5770.

[24] Y. Guo, J. Liu, Q. Yang, L. Ma, Y. Zhao, Z. Huang, X. Li, B. Dong, X.-Z. Fu, C. Zhi, *Small* **2020**, *16*, 1907341.

[25] J. Li, X. Han, D. Wang, L. Zhu, M. Ha-Thi, T. Pino, J. Arbiol, L. Wu, M. N. Ghazzal, *Angew. Chem.* **2022**, *134*, 202210242.

[26] M. Wang, J. Pu, Y. Hu, Y. Zi, Z.-G. Wu, W. Huang, *Adv. Funct. Mater.* **2024**, *34*, 2308601.

[27] M. Bacon, S. J. Bradley, T. Nann, *Part. Part. Syst. Charact.* **2014**, *31*, 415.

[28] S. Zhuo, M. Shao, S.-T. Lee, *ACS Nano* **2012**, *6*, 1059.

[29] J. N. Tiwari, A. N. Singh, S. Sultan, K. S. Kim, *Adv. Energy Mater.* **2020**, *10*, 2000280.

[30] H. Min, Y. Qi, Y. Chen, Y. Zhang, X. Han, Y. Xu, Y. Liu, J. Hu, H. Liu, Y. Li, G. Nie, *ACS Appl. Mater. Interfaces* **2019**, *11*, 32798.

[31] J. Guo, M. Guo, F. Wang, W. Jin, C. Chen, H. Liu, Y. Li, *Angew. Chem., Int. Ed.* **2020**, *59*, 16712.

[32] M. T. Gebrekidan, C. Knipfer, F. Stelzle, J. Popp, S. Will, A. Braeuer, *J. Raman Spectrosc.* **2016**, *47*, 198.

[33] H. Yan, S. Guo, F. Wu, P. Yu, H. Liu, Y. Li, L. Mao, *Angew. Chem., Int. Ed.* **2018**, *57*, 3922.

[34] R. Matsuoka, R. Sakamoto, K. Hoshiko, S. Sasaki, H. Masunaga, K. Nagashio, H. Nishihara, *J. Am. Chem. Soc.* **2017**, *139*, 3145.

[35] D. Sebastian, A. Pallikkara, H. Bhatt, H. N. Ghosh, K. Ramakrishnan, *J. Phys. Chem. C* **2022**, *126*, 11182.

[36] J. Peng, W. Gao, B. K. Gupta, Z. Liu, R. Romero-Aburto, L. Ge, L. Song, L. B. Alemany, X. Zhan, G. Gao, S. A. Vithayathil, B. A. Kaipparettu, A. A. Marti, T. Hayashi, J.-J. Zhu, P. M. Ajayan, *Nano Lett.* **2012**, *12*, 844.

[37] H. Kalita, J. Mohapatra, L. Pradhan, A. Mitra, D. Bahadur, M. Aslam, *RSC Adv.* **2016**, *6*, 23518.

[38] Z. Gan, H. Xu, Y. Hao, *Nanoscale* **2016**, *8*, 7794.

[39] X. Wen, P. Yu, Y.-R. Toh, X. Hao, J. Tang, *Adv. Opt. Mater.* **2013**, *1*, 173.

[40] G. Peng, J. E. Ellis, G. Xu, X. Xu, A. Star, *ACS Appl. Mater. Interfaces* **2016**, *8*, 7403.

[41] Z. Li, R. Ye, R. Feng, Y. Kang, X. Zhu, J. M. Tour, Z. Fang, *Adv. Mater.* **2015**, *27*, 5235.

[42] G. Cai, Z. Yu, R. Ren, D. Tang, *ACS Sens.* **2018**, *3*, 632.